

Carbon-Dots-Derived 3D Highly Nitrogen-Doped Porous Carbon Framework for High-Performance Lithium Ion Storage

Xutao Zhang,^{†,‡,§} Zhongyu Zhang,[§] Fang Hu,^{*,||} Di Li,[†] Ding Zhou,[†] Pengtao Jing,[†] Fei Du,^{*,§,¶} and Songnan Qu^{*,†,¶}

[†]State Key Laboratory of Luminescence and Applications, Changchun Institute of Optics Fine Mechanics and Physics, Chinese Academy of Sciences, No. 3888 Dong Nanhu Road, Changchun 130033, P. R. China

[‡]University of Chinese Academy of Sciences, No. 19(A) Yuquan Road, Beijing 100049, P. R. China

[§]Key Laboratory of Physics and Technology for Advanced Batteries (Ministry of Education), State Key Laboratory of Superhard Materials, College of Physics, Jilin University, No. 2699 Qianjin Street, Changchun 130012, P. R. China

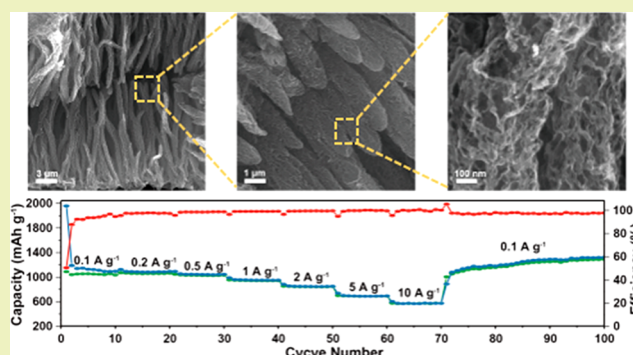
^{||}School of Materials Science and Engineering, Shenyang University of Technology, No. 111, Shenliao West Road, Shenyang 110870, P. R. China

[¶]Joint Key Laboratory of the Ministry of Education, Institute of Applied Physics and Materials Engineering, University of Macau, Avenida da Universidade, Taipa, Macau, P. R. China

Supporting Information

ABSTRACT: Nitrogen-doped porous carbon has attracted great attention in lithium ion batteries (LIBs). Herein, new three-dimensional nitrogen-doped porous carbon frameworks (N-PCFs) doped with a nitrogen content up to 19 atom % through sintering nitrogen-doped carbon dots (CDots) at 800 °C have been generated. Beneficial with regard to their large surface area and high nitrogen doping content, the N-PCFs-based LIBs display high charge/discharge capacity (1437 mAh g⁻¹ at 0.1 A g⁻¹) and considerable rate and cycling performance, manifesting their potential application for Li⁺ storage.

KEYWORDS: carbon dots, nitrogen doping, porous carbon frameworks, lithium ion batteries



INTRODUCTION

After decades of research, alkaline metal ion batteries, particularly lithium ion batteries (LIBs), have turned into a revolutionary product used in people's daily life, in items ranging from electronic products to electric vehicles.^{1–12} Anodes are of primary importance for superior electrochemical performance to obtain high power density and energy density.^{13–19} Carbon-based materials, representing low-cost and environmentally benign anode materials, have been investigated for several decades.^{20–22} Graphite is a traditional commercial anode material that has been applied in LIBs for several years. Nevertheless, low theoretical capacity becomes the bottleneck for further improvement in LIBs. Recently, much effort has been concentrated on the synthetic route to a carbonaceous anode with large specific surface area to promote shorter transfer pathways for Li⁺.^{23–27} Huang et al. prepared toastlike micro/mesoporous carbon with a surface area of 601.4 m² g⁻¹, showing 1016 mAh g⁻¹ at 0.2 A g⁻¹ for LIBs.²⁸ Ou et al. reported an ox-horn-derived 3D porous anode with 1300 m² g⁻¹ surface area for LIBs, which provided 1181 mAh g⁻¹ at 0.1 A g⁻¹.²⁹

Besides the benefits related to the porous structures, it has been demonstrated that doping with nitrogen could be helpful to improve the electrochemical capability by means of heightening the reactivity, thus increasing the electric conductivity of carbon materials.^{30–35} Lu et al. reported a porous carbon scaffold with 5.6 atom % nitrogen doping content, showing 1275 mAh g⁻¹ at 186 mA g⁻¹ for LIBs.³⁶ Pan et al. demonstrated a N-doped (6 atom %) core–sheath carbon nanotube for LIBs, which displayed 390 mAh g⁻¹ at 1.488 A g⁻¹.³⁷ Generally speaking, a top-down method from carbon sources and a bottom-up method from organic precursors are two synthesis routes for nitrogen doping.^{38–40} It is difficult to achieve a high nitrogen doping content through a top-down method due to the chemical stability of carbon sources. A bottom-up method via dehydration and carbonization from organic precursors is considered to be an effective

Received: January 21, 2019

Revised: March 17, 2019

Published: May 9, 2019

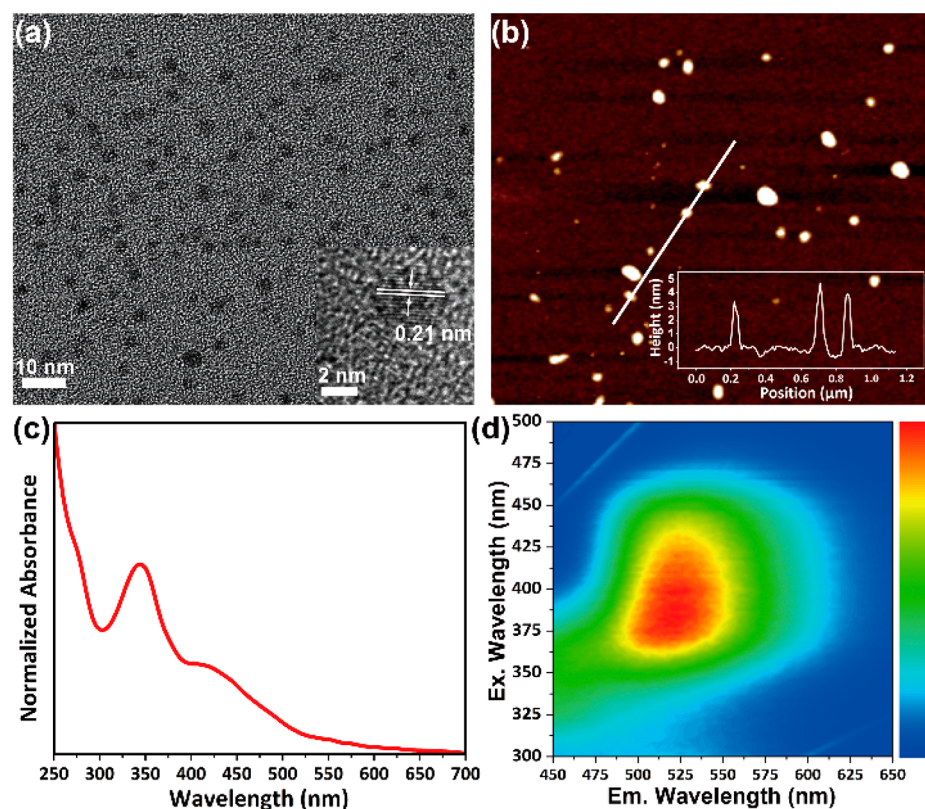


Figure 1. (a) TEM (inset: HRTEM) and (b) AFM images of CDots. (c) UV-vis absorption spectrum and (d) three-dimensional EEM fluorescence spectrum of a dilute aqueous solution of CDots.

method to realize high nitrogen doping contents by adjusting the contents of nitrogen-enriched organic precursors.

However, porous carbon materials with both high nitrogen doping contents and large surface area are scarcely realized even via a bottom-up method. Furthermore, practical applications require high specific capacity under large current density. However, high specific capacity is always accomplished within low current in the literature, which usually decreases at high current density.^{29,36,41} Therefore, preparation of a highly nitrogen-doped porous carbonaceous anode has important scientific significance for high-performance LIBs at high current density.

Carbon dots (CDots) are a newly developed carbon nanomaterial that have been researched as an innovative photoelectric material because of their nontoxicity and excellent biocompatibility characteristics.^{42–49} In alkaline metal ion batteries, CDots have been used as the composting agent, which can successfully boost the electrochemical reactivity of the composting materials. For instance, CuO@graphene CDots, VO₂@graphene CDots, MoS₂@ CDots, etc., have been studied as an anode for LIBs.^{50–52} Hou et al. proposed the first case of preparing nitrogen-free CDots derived from 3D porous carbon with sodium storage of 356.1 mAh g⁻¹ at 0.1 A g⁻¹, indicative of its potential application for energy storage.⁵³ In CDots, it is relatively easy to achieve high nitrogen doping by selecting suitable nitrogen-contained precursors via a bottom-up method. Thus, one expects to exploit a way of creating novel highly nitrogen-doped porous carbon materials based on CDots.

Herein, we first proposed and demonstrated an innovative strategy for preparing a 3D porous carbon framework with high nitrogen-doping (N-PCFs) by synthesizing nitrogen-rich

CDots. Benefiting from their large specific surface area (483.7 m² g⁻¹) and high nitrogen-doping content (19 atom %), the prepared N-PCFs-based LIBs show high reversible capacity, superior rate capability, and considerable cycling stability (1437 mAh g⁻¹ at 0.1 A g⁻¹, 840 mAh g⁻¹ at 2 A g⁻¹ after 1000 cycles), demonstrating their potential application for Li⁺ storage.

EXPERIMENTAL METHODS

Materials and Chemicals. All reagents were purchased commercially without further purification.

Preparation of CDots. A 5 g portion of citric acid and 10 g of urea were stirred vigorously until dissolved in 50 mL of DMF, and then the mixture was irradiated in a microwave instrument (500 W, 160 °C). After 3 h, the product was purified with a rotary evaporator. After centrifugation at a RCF (relative centrifugal force) of 7000g and washing several times, the final sample was subsequently freeze-dried for 12 h to acquire CDots powder.

Preparation of N-PCFs. N-PCFs were prepared by utilizing a heating rate of 5 °C min⁻¹ to calcine the freeze-dried product described above at a certain temperature (800 °C) for 1 h in a nitrogen atmosphere. Finally, the carbonized product from the previous step is preserved for subsequent steps.

Material Characterization. The electrochemical features of our samples were investigated by assembling half-cells in a glovebox protected by a nitrogen atmosphere. The as-prepared sample was mixed with polyvinylidene fluoride and Super P (8:1:1) in *N*-methylpyrrolidone and then covered copper foil. The electrode was subsequently dried at 120 °C under vacuum for 12 h. Lithium metal foils as well as Celgard 2400 were respectively utilized as counter electrodes and separator. Moreover, 1.0 M LiPF₆ in ethylene carbonate:dimethyl carbonate = 1:1 vol % was used as electrolyte. The load mass of active substance was about 0.5 mg cm⁻². Solartron Analytical is used to deliver cyclic voltammetry measurements on the

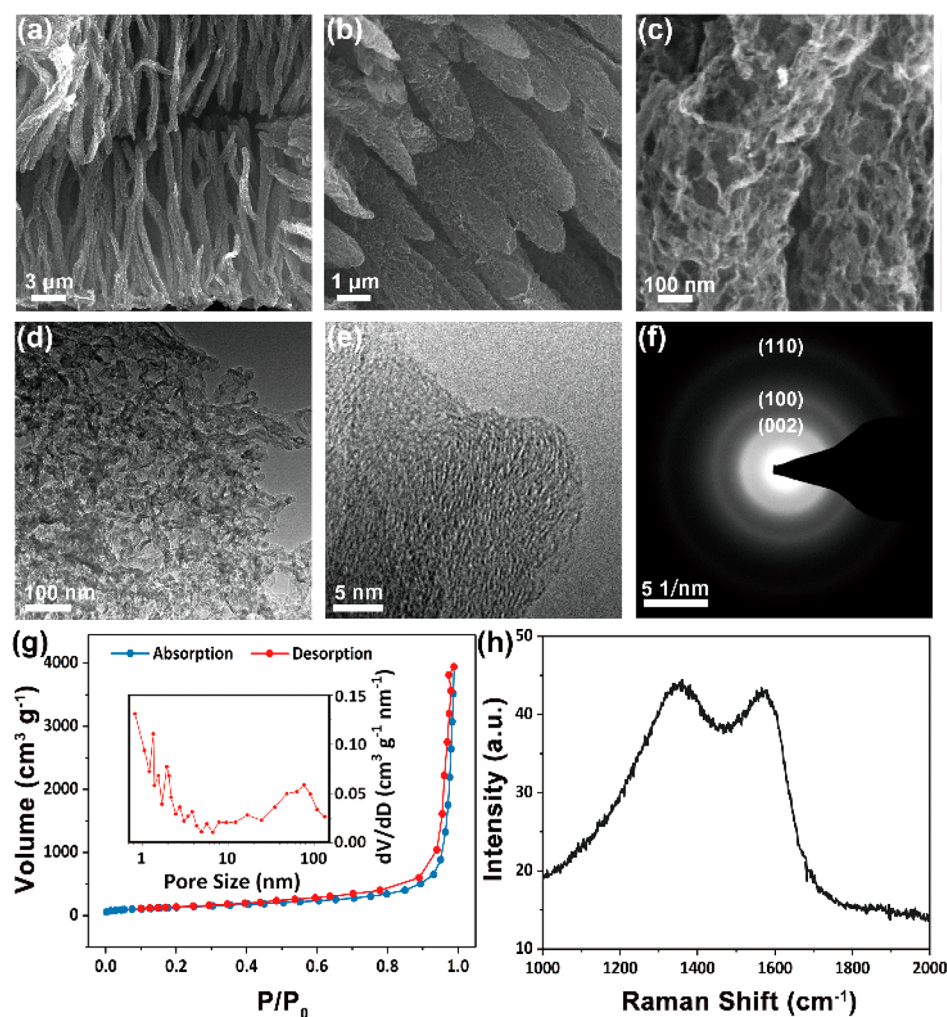


Figure 2. (a–c) SEM images and (d) TEM, (e) HRTEM, and (f) SAED images of the N-PCFs. (g) Nitrogen adsorption–desorption isotherms (inset: BJH desorption pore diameter distribution) and (h) Raman spectrum of the N-PCFs.

above cells at 0.1 mV s^{-1} in $0.01\text{--}3 \text{ V}$ to analyze the reactions between cathode and anode. The charge (ion extraction) and discharge (ion insertion) were tested under $25 \text{ }^\circ\text{C}$ through galvanostatic charge–discharge tests with a suitable current density between 0.01 and 3 V using Land CT2001A. At an amplitude of 5 mV ac voltage and from 100 kHz to 0.01 Hz , the electrochemical impedance measurement is tested using a Solartron Analytical instrument.

RESULTS AND DISCUSSION

CDots are synthesized via the microwave-assistant method detailed in the [Experimental Section](#). During the microwave-assisted synthesis, it was discovered that the color of the mixtures had transformed from achromatous to green and then red and finally dark brown [Figure S1, Supporting Information (SI)]. Subsequently, CDots were obtained by centrifugation and freeze-drying for further use. The morphology of the as-prepared CDots is investigated by transmission electronic microscopy (TEM) and atomic force microscopy (AFM), as illustrated in parts a and b of [Figure 1](#), respectively. [Figure 1a](#) shows that CDots are uniformly dispersed in $3\text{--}5 \text{ nm}$. The inset of [Figure 1a](#) show the high-resolution transmission electronic microscopy of a single carbon dot, indicating that the interplanar spacing is 0.21 nm , which can be assigned to the (100) plane. A dilute aqueous solution of CDots indicates

absorption bands peaking at 335 and 415 nm , being representative of aromatic π systems and extended π -conjugated structures ([Figure 1c](#)). The excitation–emission matrix (EEM) of CDots shows excitation-dependent fluorescence emissions in the range of $500\text{--}540 \text{ nm}$ under excitation at $370\text{--}420 \text{ nm}$ ([Figure 1d](#)).

The N-PCFs were further prepared by first presintering the CDots at $200 \text{ }^\circ\text{C}$ for 1 h and then heating up to $800 \text{ }^\circ\text{C}$ for 2 h . The morphology of the as-prepared N-PCFs was researched by scanning electron microscopy (SEM) and TEM, accordingly. SEM pictures of the N-PCFs in distinctive magnifications clearly exhibit fiber arrays with hierarchical pores, which are composed of cross-linked nanosheets ([Figure 2a–c](#)). The hierarchical pores with embedding caves can provide more transport capacity for Li^+ , which is beneficial for faster ion transfer. The corresponding TEM and HRTEM images of N-PCFs shown in [Figure 2d,e](#) exhibit random cross-linked carbon nanosheets, forming abundant unordered micro- and mesopore. A selected area electron diffraction pattern indicates that the as-prepared N-PCFs have a carbon structure with d -spacing of 0.12 , 0.21 , and 0.34 nm , relating to the (002), (100) and (110) planes, respectively ([Figure 2f](#)).

To further examine the surface area of the N-PCFs, nitrogen adsorption–desorption isotherms were determined ([Figure 2g](#)). The Brunauer–Emmett–Teller (BET) surface area was

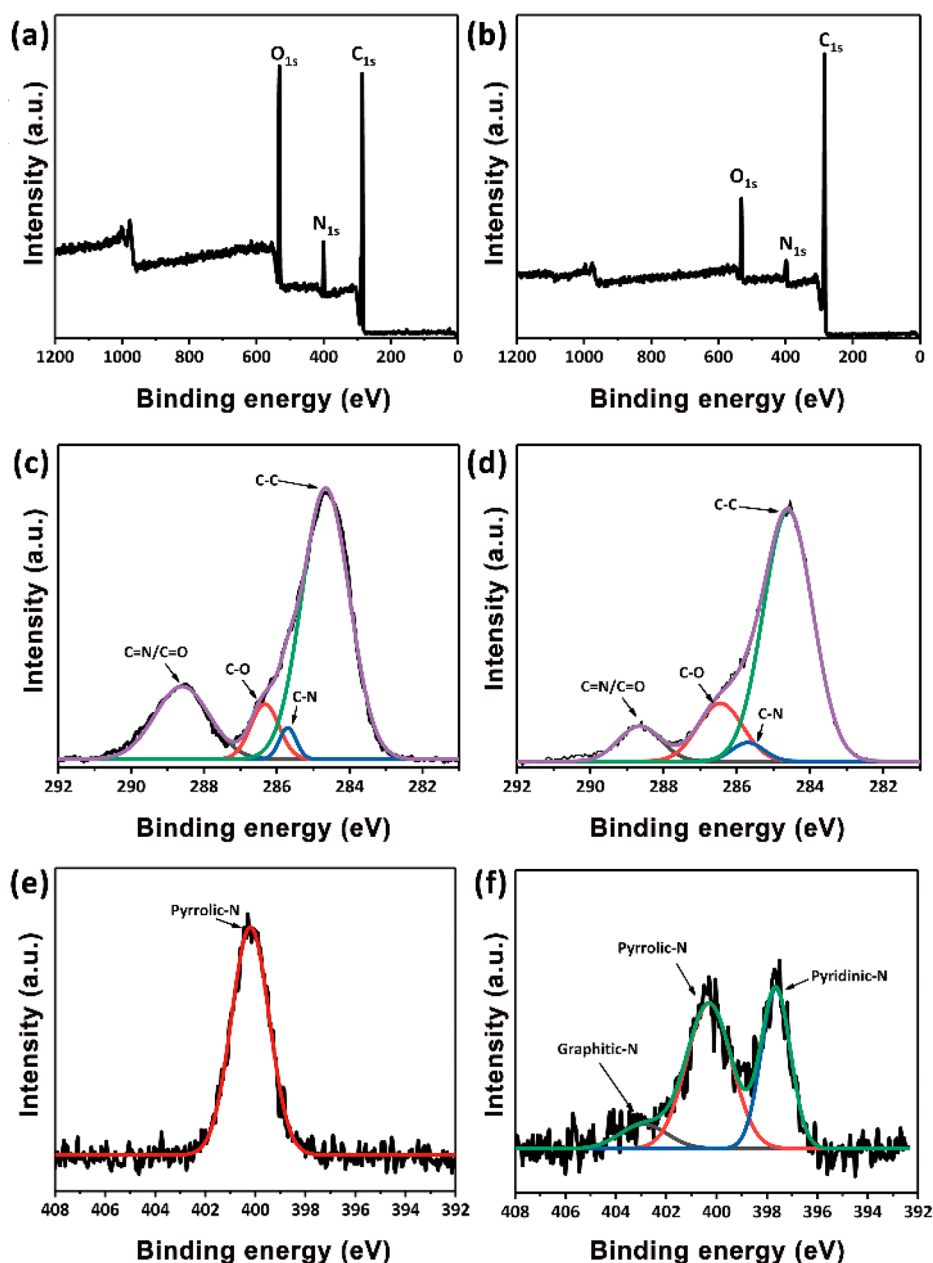


Figure 3. XPS survey spectra (a) and high-resolution XPS spectrum in the C_{1s} region (c) and N_{1s} region (e) of CDots. XPS survey spectra (b) and high-resolution XPS spectrum in the C_{1s} region (d) and N_{1s} region (f) of N-PCFs.

up to $483.7 \text{ m}^2 \text{ g}^{-1}$. The N-PCFs have a typical IV N_2 -adsorption isotherm of a mesoporous material, with H1-type hysteresis loops at $P/P_0 = 0.7\text{--}0.95$. The inset of Figure 2g is the average pore diameter distribution calculated according to desorption branches stated in the Barret–Joyner–Halenda (BJH) model. It can be seen from the pore diameter distribution plots that N-PCFs have several peaks in the range of 0.5–100 nm, indicating the hierarchical porous structure of the N-PCFs. Those micropores may be primarily formed during cross-linking between CDots. Meanwhile, the pore size distribution of 50–100 nm agrees well with the observed macropores, which should be due to the accumulation of CDots. The X-ray diffraction (XRD) pattern of N-PCFs illustrates two typical peaks near 26° and 42° , which combined with the (002) and (100) planes in a graphite-like structure (Figure S2, SI). As shown in Figure 2h, two typical

Raman peaks are being observed for the N-PCFs. The G-band is located at 1593 cm^{-1} , corresponding to the same graphite in the E_{2g} mode, and the D-band at 1325 cm^{-1} is corresponding to the defective inducement mode. The high intensity of the D-band suggests low graphitization, which may be inherited from the chemical composition of the CDots precursors.

To learn the chemical structure changes, X-ray photoelectron spectroscopy (XPS) was measured for CDots and the N-PCFs. XPS spectra of the CDots and the prepared N-PCFs (Figure 3a,b) have peaks at 284.0, 400.0, and 530.4 eV, which corresponded to C_{1s} , N_{1s} , and O_{1s} , respectively. The high resolution C_{1s} XPS spectra (Figure 3c,d) has peaks at 284.6, 285.7, 286.6, and 288.3 eV, corresponding to $sp^2 \text{ C}$, C–N, C–O, and C=N/C=O, respectively. Nitrogen contents of the as-prepared N-PCFs are 19 atom %. Peaks of pyridinic N (at 398.0 eV), pyrrolic or pyridonic N (at 399.7 eV), and graphite

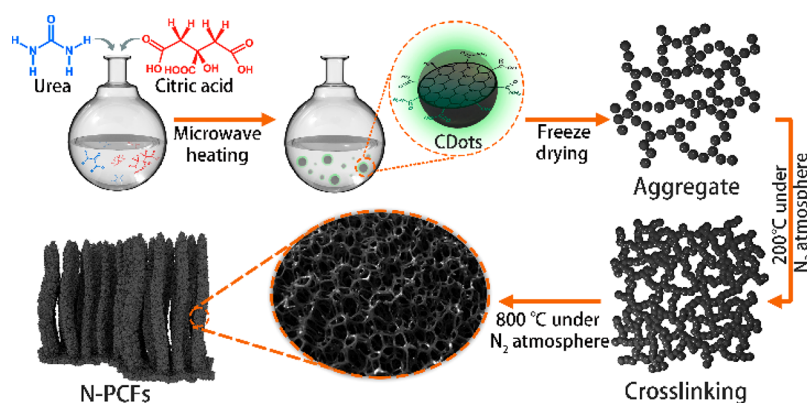


Figure 4. A possible growth mechanism for the CDots and subsequently synthesized N-PCFs.

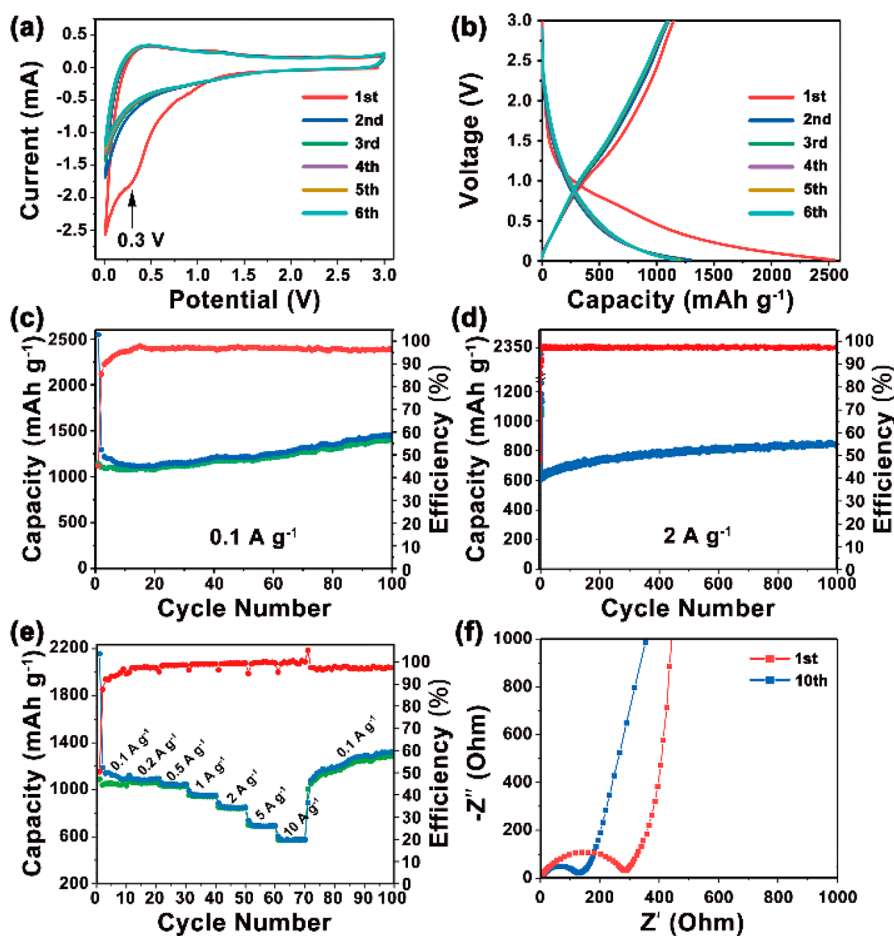


Figure 5. (a) Cyclic voltammograms at 0.1 mVs⁻¹ of LIBs. (b) Charge/discharge curves at 0.1 A g⁻¹ of LIBs. (c) Cycle performance and Coulombic efficiency at 0.1 A g⁻¹. (d) Cycle performance and Coulombic efficiency at 2 A g⁻¹. (e) Capacity over cycling at different rates (from 0.1 to 10 A g⁻¹). (f) Nyquist plots of LIB in their initial cycle (red) and after 10 cycles (blue).

N (at 402.5 eV) were obtained by deconvolution of high-resolution N_{1s} XPS spectra. On the basis of the XPS analysis, it can be obviously observed that the N-containing species in CDots were converted from pyrrolic-N to pyridinic-N and graphite-N after 800 °C sintering, indicating nitrogen-doping within the N-PCFs. Comparing to pyrrolic-N, pyridinic-N could provide more reactive sites.³⁰

On the basis of the experimental data above, a possible formation mechanism of the N-PCFs was proposed in Figure 4. Lyophilization leads to loose accumulation of the CDots. At 200 °C heating, cross-linking between CDots can happen,

which prevents collapsing of CDots and maintains the mesospaces between CDots. During 800 °C heating, the cross-linked CDots were further carbonized, forming a self-supporting 3D porous nitrogen-doped carbon framework. During the presintering and carbonization process, pyrrolic-N in CDots become pyridinic-N and graphite-N. Due to the self-supporting porous structural features, a high degree of nitrogen-doping (19 atom %), high surface area (483.7 m² g⁻¹), and abundant micro/mesopores, rapid ion diffusion and adsorption in the N-PCFs are expected, which are primarily important for LIBs.

Electrochemical properties of N-PCFs in LIBs are studied by the standard half-cell configuration. Figure 5 shows the cyclic voltammograms of the N-PCFs anode, which were measured in the first six cycles at 0.1 mV s^{-1} . During the initial cycle of LIBs (Figure 5a), a reduction peak at 0.3 V is clearly detected. This broad peak corresponded to the electrolyte decomposition and the formation of a solid electrolyte interface (SEI) film. The formation of a SEI and the irretrievable insertion of Li^+ into the carbonaceous structure led an irreversible capacity decrease. The cathode peak at about 0.01 V is caused by Li^+ insertion into carbonaceous materials. During the anode process, broad peaks of LIBs can be found in the first and subsequent cycles. These broad peaks demonstrate that Li^+ extract from N-PCFs occurs over a broad range.

After the first scan, CV curves are nearly overlapping, indicating that the N-PCFs had good cyclic performance during the inset-extract stage. Figure 5b shows corresponding galvanostatic charge/discharge performance of N-PCFs in a lithium battery system between 0.01 and 3 V at 0.1 A g^{-1} . The initial reversible capacity and Coulombic efficiency of the N-PCFs anode were 1145 mAh g^{-1} and 51% for LIBs. The Coulombic efficiency for the N-PCFs anode rose rapidly beyond 90% after the first few cycles. The large amount of irreversible capacity loss for LIBs was the cause of the SEI layer and other adverse reactions, for instance, the corrosion-like reaction of Li_xC_6 , the reaction between Li^+ and the surface functional groups, the superfine pores insertion, and electrolyte decomposition. In addition to the traditional graphite intercalation mechanism, many distinctive Li^+ storage methods in N-PCFs may exist. Supermicropores and small mesopores successfully act as containers for Li^+ storage.⁵⁴

In addition, an active position for Li^+ adsorption and diffusion exists on the edge of three-dimensional corrugated N-PCFs. Furthermore, as a result of the high binding energy at heteroatom positions, it is efficient and easy to absorb Li^+ .⁵⁵ In the discharge process, Li^+ are trapped onto the N-PCFs edges, the surface defects of microporous and mesoporous, and the heteroatom sites at the sloping voltage region. In the process of charge, Li^+ are free from the N-PCFs anode. It is noteworthy that the charge capacity in the initial cycle for LIBs demonstrates the good electrochemical reversibility of the N-PCFs.

As shown in Figure 5c,d, the cycling capability of N-PCFs was appraised at 0.1 and 2 A g^{-1} from 0.01 to 3 V. The N-PCFs anodes show capacity increasing in LIBs. This interesting phenomenon should be considered as the activation of anode.^{24,35,41,55} In LIBs, the capacity of N-PCFs displays a growing trend from 1130 to 1437 mAh g^{-1} at 0.1 A g^{-1} and from 620 to 840 mAh g^{-1} at 2 A g^{-1} , owing to the activating procedure of the porous anode and the appropriate electrolyte. Notably, the capacity is reduced in the first 10 cycles, but it is going to grow again in subsequent cycles and delivers a continuous capacity increase when comparing the 10th cycle with the 1000th cycle under 2 A g^{-1} .

During the first few cycles, large quantities of Li^+ are embedded into the interlayers of the as-prepared N-PCFs, adsorbed at heteroatoms or filled in the supermicropores and small mesopores, which may impede Li^+ transfer from electrode to electrolyte, leading to a reduction in capacity.⁵² In subsequent cycles, the layer spacing of the carbon sheets becomes larger, which facilitates the extraction of Li^+ from the N-PCFs.⁵⁶ Meanwhile, the unique architecture of as-prepared N-PCFs can reduce the diffusion length of ions,⁵⁷ allowing for

adequate contact of electrode and electrolyte, contributing to the capacity increasing after several cycles.

Moreover, the N-PCFs anode demonstrates impressive high-rate performance for Li^+ systems even at very high current densities (as showed in Figure 5e). During the testing process, LIBs were cycled at 0.1 A g^{-1} for 10 cycles and then for 10 cycles at distinct currents from 0.2 to 10 A g^{-1} . Reversible capacities were from 572 to 1322 mAh g^{-1} for LIBs. In particular, the N-PCFs anode held 572 mAh g^{-1} even at 10 A g^{-1} , much higher than other anodes in corresponding LIBs.^{29,36,41} The favorable rate performance should be linked to the particular structure of N-PCFs: large specific surface area, multidimensional electronic transportation pathway, and high nitrogen doping content. It could be stated that the as-prepared N-PCFs exhibit incredibly stable cycling stability. The detailed reaction kinetics of the N-PCFs in LIBs was explored using electrochemical impedance spectroscopy (EIS) at 10 mV amplitude from 10 MHz to 0.01 Hz .

Figure 5f illustrates a typical Nyquist plot of the N-PCFs anodes, and the impedance spectra consisted of a concave semicircle and an oblique line. The semicircle corresponds to SEI impedance, while the oblique line corresponds to ion diffusion. The N-PCF formed by carbon dots acts as a channel for electron transport, and abundant nanopores in N-PCF can also be used as collectors for Li^+ . The large surface area provides enough electrode/electrolyte interfaces, which can better absorb Li^+ and facilitate fast charge transfer reactions. The hierarchical porous structures lower the transfer distance of Li^+ , and the nanopores on the surface of N-PCFs can provide a rapid transit route for the Li^+ . Cross-linked carbon fiber networks, on the other hand, provide a continuous path for electron transmission. Moreover, nitrogen doping in the N-PCFs could improve the electrochemical responsiveness and electronic conductivity, further contributing to its exceptional properties.

To reveal the origin of the superior rate capability of N-PCFs, CV profiles at various scanning rates were collected in the potential region of 0.01 – 3.0 V to evaluate its potential capacitive contribution, as displayed in Figure 6a. The total stored charge can be separated into three components: the Faradaic contribution from the ions insertion process, the Faradaic contribution from the charge-transfer process with surface atoms, and the non-Faradaic contribution from the double layer effect.⁵⁸ The measured current (i) and the scanning rate (ν) obey eq 1⁵⁹

$$i = a\nu^b \quad (1)$$

where a and b are variable positive numbers. The b value can be determined by the slope of the $\log(\nu)$ – $\log(i)$ plots and for an ideal diffusion-controlled behavior, the value is 0.5. Otherwise, a value of 1.0 corresponds to a capacitive process. As in Figure 6b, the b value of 0.79 and 0.93 for cathodic peak potential of 1.50 V and anodic peaks potential of 1.50 V , respectively, can be quantified at scan rates from 0.1 to 1 mV s^{-1} , suggesting the contribution of capacitive behavior in addition to Faradic reaction.

The total capacitive contribution at a certain scan rate could be quantified on the base of separating the specific contribution from the capacitive and diffusion-controlled charge at a fixed voltage. Quantitatively, these two components can be discriminated by evaluating the current response (i) at a fixed potential (V) via eq 2⁶⁰

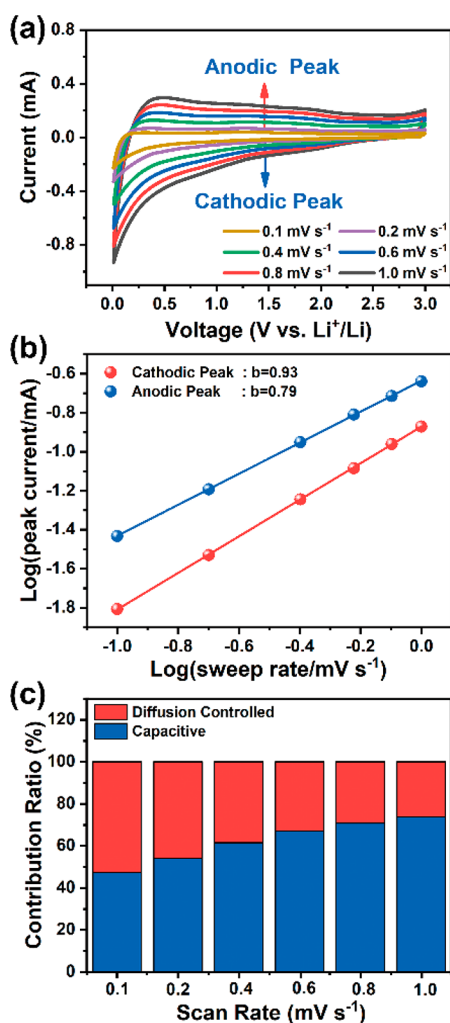


Figure 6. Kinetics analysis of the electrochemical behavior of N-PCFs: (a) CV curves at various scan rates and (b) linear relationship of $\log(i)$ and $\log(v)$. (c) Contribution ratio of the capacitive and diffusion-controlled charge versus scan rate.

$$i(V)/v^{1/2} = k_1v + k_2v^{1/2} \quad (2)$$

where k_1v and $k_2v^{1/2}$ originate from the capacitive and diffusion-controlled effects, respectively. The values of k_1v and $k_2v^{1/2}$ can be determined from the slope and the y -axis intercept point of the linear function between $i(V)/v^{1/2}$ and $v^{1/2}$, respectively. Figure S5 (SI) shows the typical voltage profile for the capacitive current (shaded region) in comparison with the total current of the N-PCFs electrode at a scan rate of 0.8 mV s^{-1} , as an example, for which the capacitive contribution is ca. 71%. The normalized results (Figure 6c) indicate that the capacitance effect plays a growing role as the scanning rate increases, and the capacitive contribution finally reaches a high value of $\sim 74\%$ at 1 mV s^{-1} .

CONCLUSION

In conclusion, we have developed a 3D nitrogen-doped porous carbon framework (N-PCFs) with a nitrogen-doping content up to 19% through sintering nitrogen-doped carbon dots (CDots) at $800 \text{ }^\circ\text{C}$. Benefiting from the large surface area and high nitrogen doping concentration, N-PCFs-based LIBs show high capacity, superior rate capability, and stability of cycles. After a thousand cycles, the performance of the LIBs attains

840 mAh g^{-1} at 2 A g^{-1} . Our study demonstrated that the CDots-derived N-PCFs are encouraging LIBs anode materials with excellent reversibility and highly stable cycling performance. In addition, we expect that the N-PCFs also can be applied for supercapacitor, adsorbent, catalyst, and hydrogen storage, and this proposed method is also promising to develop novel PCFs with B, N, S, or P doping from other CDots precursors.

ASSOCIATED CONTENT

Supporting Information

The Supporting Information is available free of charge on the ACS Publications website at DOI: 10.1021/acssuschemeng.9b00407.

Synthesis process, SEM, TEM, and energy dispersive spectrometry (EDS) of CDots; XRD spectra, EDS, elemental analysis, and specific capacity at different current densities of N-PCFs; and contribution of the capacitive current in N-PCFs (PDF)

AUTHOR INFORMATION

Corresponding Authors

*F.H. e-mail: hufang25@126.com.

*F.D. e-mail: dufei@jlu.edu.cn.

*S.Q. e-mail: songnanqu@um.edu.mo.

ORCID

Xutao Zhang: 0000-0002-5588-0311

Fei Du: 0000-0001-6413-0689

Songnan Qu: 0000-0003-4159-096X

Notes

The authors declare no competing financial interest.

ACKNOWLEDGMENTS

This work has been supported by the National Natural Science Foundation of China (project No. 51602304); Jilin Province Science and Technology Research Projects No. 20180101190JC, 20170101191JC, 20170101042JC, 20160520008JH, and 20150519003JH; and the Youth Innovation Promotion Association of CAS.

REFERENCES

- (1) Wu, Z.-S.; Ren, W.; Wen, L.; Gao, L.; Zhao, J.; Chen, Z.; Zhou, G.; Li, F.; Cheng, H.-M. Graphene Anchored with Co_3O_4 Nanoparticles as Anode of Lithium Ion Batteries with Enhanced Reversible Capacity and Cyclic Performance. *ACS Nano* **2010**, *4* (6), 3187–3194.
- (2) Goodenough, J. B.; Park, K.-S. The Li-Ion Rechargeable Battery: A Perspective. *J. Am. Chem. Soc.* **2013**, *135* (4), 1167–1176.
- (3) Xu, Y.; Zhu, Y.; Liu, Y.; Wang, C. Electrochemical Performance of Porous Carbon/Tin Composite Anodes for Sodium-Ion and Lithium-Ion Batteries. *Adv. Energy Mater.* **2013**, *3* (1), 128–133.
- (4) Augustyn, V.; Simon, P.; Dunn, B. Pseudocapacitive oxide materials for high-rate electrochemical energy storage. *Energy Environ. Sci.* **2014**, *7* (5), 1597–1614.
- (5) Lin, T.; Chen, I.-W.; Liu, F.; Yang, C.; Bi, H.; Xu, F.; Huang, F. Nitrogen-doped mesoporous carbon of extraordinary capacitance for electrochemical energy storage. *Science* **2015**, *350* (6267), 1508–1513.
- (6) Wang, D.; Bie, X.; Fu, Q.; Dixon, D.; Bramnik, N.; Hu, Y. S.; Fauth, F.; Wei, Y.; Ehrenberg, H.; Chen, G.; Du, F. Sodium vanadium titanium phosphate electrode for symmetric sodium-ion batteries with high power and long lifespan. *Nat. Commun.* **2017**, *8*, 15888–15894.

- (7) He, C.; Wu, S.; Zhao, N.; Shi, C.; Liu, E.; Li, J. Carbon-Encapsulated Fe₃O₄ Nanoparticles as a High-Rate Lithium Ion Battery Anode Material. *ACS Nano* **2013**, *7* (5), 4459–4469.
- (8) Wang, H.; Dai, H. Strongly coupled inorganic-nano-carbon hybrid materials for energy storage. *Chem. Soc. Rev.* **2013**, *42* (7), 3088–3113.
- (9) Ding, J.; Wang, H.; Li, Z.; Kohandehghan, A.; Cui, K.; Xu, Z.; Zahiri, B.; Tan, X.; Lotfabad, E. M.; Olsen, B. C.; Mitlin, D. Carbon Nanosheet Frameworks Derived from Peat Moss as High Performance Sodium Ion Battery Anodes. *ACS Nano* **2013**, *7* (12), 11004–11015.
- (10) Xu, J.; Wang, M.; Wickramaratne, N. P.; Jaroniec, M.; Dou, S.; Dai, L. High-Performance Sodium Ion Batteries Based on a 3D Anode from Nitrogen-Doped Graphene Foams. *Adv. Mater.* **2015**, *27* (12), 2042–2048.
- (11) Jian, Z.; Luo, W.; Ji, X. Carbon Electrodes for K-Ion Batteries. *J. Am. Chem. Soc.* **2015**, *137* (36), 11566–11569.
- (12) Share, K.; Cohn, A. P.; Carter, R.; Rogers, B.; Pint, C. L. Role of Nitrogen-Doped Graphene for Improved High-Capacity Potassium Ion Battery Anodes. *ACS Nano* **2016**, *10* (10), 9738–9744.
- (13) Kim, H.; Kim, H.; Ding, Z.; Lee, M. H.; Lim, K.; Yoon, G.; Kang, K. Recent Progress in Electrode Materials for Sodium-Ion Batteries. *Adv. Energy Mater.* **2016**, *6* (19), 1600943–1600980.
- (14) Luo, W.; Shen, F.; Bommier, C.; Zhu, H.; Ji, X.; Hu, L. Na-Ion Battery Anodes: Materials and Electrochemistry. *Acc. Chem. Res.* **2016**, *49* (2), 231–240.
- (15) Goodenough, J. B. Evolution of Strategies for Modern Rechargeable Batteries. *Acc. Chem. Res.* **2013**, *46* (5), 1053–1061.
- (16) Goriparti, S.; Miele, E.; De Angelis, F.; Di Fabrizio, E.; Proietti Zaccaria, R.; Capiglia, C. Review on recent progress of nanostructured anode materials for Li-ion batteries. *J. Power Sources* **2014**, *257*, 421–443.
- (17) Zhang, Q.; Uchaker, E.; Candelaria, S. L.; Cao, G. Nanomaterials for energy conversion and storage. *Chem. Soc. Rev.* **2013**, *42* (7), 3127–3171.
- (18) Kundu, D.; Talaie, E.; Duffort, V.; Nazar, L. F. The Emerging Chemistry of Sodium Ion Batteries for Electrochemical Energy Storage. *Angew. Chem., Int. Ed.* **2015**, *54* (11), 3431–3448.
- (19) Zhang, X.-Y.; Sun, S.-H.; Sun, X.-J.; Zhao, Y.-R.; Chen, L.; Yang, Y.; Lü, W.; Li, D.-B. Plasma-induced, nitrogen-doped graphene-based aerogels for high-performance supercapacitors. *Light: Sci. Appl.* **2016**, *5*, e16130.
- (20) Flandrois, S.; Simon, B. Carbon materials for lithium-ion rechargeable batteries. *Carbon* **1999**, *37* (2), 165–180.
- (21) Candelaria, S. L.; Shao, Y.; Zhou, W.; Li, X.; Xiao, J.; Zhang, J.-G.; Wang, Y.; Liu, J.; Li, J.; Cao, G. Nanostructured carbon for energy storage and conversion. *Nano Energy* **2012**, *1* (2), 195–220.
- (22) Su, D. S.; Schlögl, R. Nanostructured Carbon and Carbon Nanocomposites for Electrochemical Energy Storage Applications. *ChemSusChem* **2010**, *3* (2), 136–168.
- (23) Hou, J.; Cao, C.; Idrees, F.; Ma, X. Hierarchical Porous Nitrogen-Doped Carbon Nanosheets Derived from Silk for Ultrahigh-Capacity Battery Anodes and Supercapacitors. *ACS Nano* **2015**, *9* (3), 2556–2564.
- (24) Qie, L.; Chen, W.-M.; Wang, Z.-H.; Shao, Q.-G.; Li, X.; Yuan, L.-X.; Hu, X.-L.; Zhang, W.-X.; Huang, Y.-H. Nitrogen-Doped Porous Carbon Nanofiber Webs as Anodes for Lithium Ion Batteries with a Superhigh Capacity and Rate Capability. *Adv. Mater.* **2012**, *24* (15), 2047–2050.
- (25) Hou, Y.; Li, J.; Wen, Z.; Cui, S.; Yuan, C.; Chen, J. N-doped graphene/porous g-C₃N₄ nanosheets supported layered-MoS₂ hybrid as robust anode materials for lithium-ion batteries. *Nano Energy* **2014**, *8*, 157–164.
- (26) Lotfabad, E. M.; Ding, J.; Cui, K.; Kohandehghan, A.; Kalisvaart, W. P.; Hazelton, M.; Mitlin, D. High-Density Sodium and Lithium Ion Battery Anodes from Banana Peels. *ACS Nano* **2014**, *8* (7), 7115–7129.
- (27) Wang, S.; Xia, L.; Yu, L.; Zhang, L.; Wang, H.; Lou, X. W. Free-Standing Nitrogen-Doped Carbon Nanofiber Films: Integrated Electrodes for Sodium-Ion Batteries with Ultralong Cycle Life and Superior Rate Capability. *Adv. Energy Mater.* **2016**, *6* (7), 1502217–1502223.
- (28) Huang, H.; Cheng, C.; Liang, S.; Liang, C.; Xia, Y.; Gan, Y.; Zhang, J.; Tao, X.; Zhang, W. Toast-like porous carbon derived from one-step reduction of CaCO₃ for electrochemical lithium storage. *Carbon* **2018**, *130*, 559–565.
- (29) Ou, J.; Zhang, Y.; Chen, L.; Zhao, Q.; Meng, Y.; Guo, Y.; Xiao, D. Nitrogen-rich porous carbon derived from biomass as a high performance anode material for lithium ion batteries. *J. Mater. Chem. A* **2015**, *3* (12), 6534–6541.
- (30) Cirić-Marjanović, G.; Pašti, I.; Mentus, S. One-dimensional nitrogen-containing carbon nanostructures. *Prog. Mater. Sci.* **2015**, *69*, 61–182.
- (31) Bulusheva, L. G.; Okotrub, A. V.; Kurenya, A. G.; Zhang, H.; Zhang, H.; Chen, X.; Song, H. Electrochemical properties of nitrogen-doped carbon nanotube anode in Li-ion batteries. *Carbon* **2011**, *49* (12), 4013–4023.
- (32) Li, Y. F.; Zhou, Z.; Wang, L. B. CN(x) nanotubes with pyridineline structures: p-type semiconductors and Li storage materials. *J. Chem. Phys.* **2008**, *129* (10), 104703–104707.
- (33) Su, F.; Poh, C. K.; Chen, J. S.; Xu, G.; Wang, D.; Li, Q.; Lin, J.; Lou, X. W. Nitrogen-containing microporous carbon nanospheres with improved capacitive properties. *Energy Environ. Sci.* **2011**, *4* (3), 717–724.
- (34) Reddy, A. L. M.; Srivastava, A.; Gowda, S. R.; Gullapalli, H.; Dubey, M.; Ajayan, P. M. Synthesis Of Nitrogen-Doped Graphene Films For Lithium Battery Application. *ACS Nano* **2010**, *4* (11), 6337–6342.
- (35) Wu, Z.-S.; Ren, W.; Xu, L.; Li, F.; Cheng, H.-M. Doped Graphene Sheets As Anode Materials with Superhigh Rate and Large Capacity for Lithium Ion Batteries. *ACS Nano* **2011**, *5* (7), 5463–5471.
- (36) Lu, H.; Chen, R.; Hu, Y.; Wang, X.; Wang, Y.; Ma, L.; Zhu, G.; Chen, T.; Tie, Z.; Jin, Z.; Liu, J. Bottom-up synthesis of nitrogen-doped porous carbon scaffolds for lithium and sodium storage. *Nanoscale* **2017**, *9* (5), 1972–1977.
- (37) Pan, Z.; Ren, J.; Guan, G.; Fang, X.; Wang, B.; Doo, S.-G.; Son, I. H.; Huang, X.; Peng, H. Synthesizing Nitrogen-Doped Core-Sheath Carbon Nanotube Films for Flexible Lithium Ion Batteries. *Adv. Energy Mater.* **2016**, *6* (11), 1600271–1600276.
- (38) Zhou, J.; Zhou, H.; Tang, J.; Deng, S.; Yan, F.; Li, W.; Qu, M. Carbon dots doped with heteroatoms for fluorescent bioimaging: a review. *Microchim. Acta* **2017**, *184* (2), 343–368.
- (39) Sun, Z.; James, D. K.; Tour, J. M. Graphene Chemistry: Synthesis and Manipulation. *J. Phys. Chem. Lett.* **2011**, *2* (19), 2425–2432.
- (40) Yang, Y.; Han, C.; Jiang, B.; Iocozzia, J.; He, C.; Shi, D.; Jiang, T.; Lin, Z. Graphene-based materials with tailored nanostructures for energy conversion and storage. *Mater. Sci. Eng., R* **2016**, *102*, 1–72.
- (41) Zhang, W.; Yin, J.; Lin, Z.; Lin, H.; Lu, H.; Wang, Y.; Huang, W. Facile preparation of 3D hierarchical porous carbon from lignin for the anode material in lithium ion battery with high rate performance. *Electrochim. Acta* **2015**, *176*, 1136–1142.
- (42) Qu, S.; Wang, X.; Lu, Q.; Liu, X.; Wang, L. A Biocompatible Fluorescent Ink Based on Water-Soluble Luminescent Carbon Nanodots. *Angew. Chem., Int. Ed.* **2012**, *51* (49), 12215–12218.
- (43) Lim, S. Y.; Shen, W.; Gao, Z. Carbon quantum dots and their applications. *Chem. Soc. Rev.* **2015**, *44* (1), 362–381.
- (44) Sun, Y.-P.; Zhou, B.; Lin, Y.; Wang, W.; Fernando, K. A. S.; Pathak, P.; Mezziani, M. J.; Harruff, B. A.; Wang, X.; Wang, H.; Luo, P. G.; Yang, H.; Kose, M. E.; Chen, B.; Veca, L. M.; Xie, S.-Y. Quantum-Sized Carbon Dots for Bright and Colorful Photoluminescence. *J. Am. Chem. Soc.* **2006**, *128* (24), 7756–7757.
- (45) Qu, D.; Zheng, M.; Li, J.; Xie, Z.; Sun, Z. Tailoring color emissions from N-doped graphene quantum dots for bioimaging applications. *Light: Sci. Appl.* **2015**, *4*, e364.
- (46) Li, D.; Han, D.; Qu, S.-N.; Liu, L.; Jing, P.-T.; Zhou, D.; Ji, W.-Y.; Wang, X.-Y.; Zhang, T.-F.; Shen, D.-Z. Supra-(carbon nanodots)

with a strong visible to near-infrared absorption band and efficient photothermal conversion. *Light: Sci. Appl.* **2016**, *5*, e16120.

(47) Bao, X.; Yuan, Y.; Chen, J.; Zhang, B.; Li, D.; Zhou, D.; Jing, P.; Xu, G.; Wang, Y.; Hola, K.; Shen, D.; Wu, C.; Song, L.; Liu, C.; Zboril, R.; Qu, S. In vivo theranostics with near-infrared-emitting carbon dots-highly efficient photothermal therapy based on passive targeting after intravenous administration. *Light: Sci. Appl.* **2018**, *7*, 91–101.

(48) Gao, J.; Zhu, M.; Huang, H.; Liu, Y.; Kang, Z. Advances, challenges and promises of carbon dots. *Inorg. Chem. Front.* **2017**, *4*, 1963–1986.

(49) Li, H.; Kang, Z.; Liu, Y.; Lee, S. Carbon nanodots: synthesis, properties and applications. *J. Mater. Chem.* **2012**, *22*, 24230–24253.

(50) Zhu, C.; Chao, D.; Sun, J.; Bacho, I. M.; Fan, Z.; Ng, C. F.; Xia, X.; Huang, H.; Zhang, H.; Shen, Z. X.; Ding, G.; Fan, H. J. Enhanced Lithium Storage Performance of CuO Nanowires by Coating of Graphene Quantum Dots. *Adv. Mater. Interfaces* **2015**, *2* (2), 1400499–1400504.

(51) Chao, D.; Zhu, C.; Xia, X.; Liu, J.; Zhang, X.; Wang, J.; Liang, P.; Lin, J.; Zhang, H.; Shen, Z. X.; Fan, H. J. Graphene Quantum Dots Coated VO₂ Arrays for Highly Durable Electrodes for Li and Na Ion Batteries. *Nano Lett.* **2014**, *15* (1), 565–573.

(52) Guo, J.; Zhu, H.; Sun, Y.; Tang, L.; Zhang, X. Boosting the lithium storage performance of MoS₂ with graphene quantum dots. *J. Mater. Chem. A* **2016**, *4* (13), 4783–4789.

(53) Hou, H.; Banks, C. E.; Jing, M.; Zhang, Y.; Ji, X. Carbon Quantum Dots and Their Derivative 3D Porous Carbon Frameworks for Sodium-Ion Batteries with Ultralong Cycle Life. *Adv. Mater.* **2015**, *27* (47), 7861–7866.

(54) Song, R.; Song, H.; Zhou, J.; Chen, X.; Wu, B.; Yang, H. Y. Hierarchical porous carbon nanosheets and their favorable high-rate performance in lithium ion batteries. *J. Mater. Chem.* **2012**, *22* (24), 12369–12374.

(55) Tian, L.-L.; Li, S.-B.; Zhang, M.-J.; Li, S.-K.; Lin, L.-P.; Zheng, J.-X.; Zhuang, Q.-C.; Amine, K.; Pan, F. Cascading Boost Effect on the Capacity of Nitrogen-Doped Graphene Sheets for Li- and Na-Ion Batteries. *ACS Appl. Mater. Interfaces* **2016**, *8* (40), 26722–26729.

(56) Wen, Y.; He, K.; Zhu, Y.; Han, F.; Xu, Y.; Matsuda, I.; Ishii, Y.; Cumings, J.; Wang, C. Expanded graphite as superior anode for sodium-ion batteries. *Nat. Commun.* **2014**, *5*, 4033–4042.

(57) Roy, P.; Srivastava, S. K. Nanostructured anode materials for lithium ion batteries. *J. Mater. Chem. A* **2015**, *3* (6), 2454–2484.

(58) Wang, J.; Polleux, J.; Lim, J.; Dunn, B. Pseudocapacitive Contributions to Electrochemical Energy Storage in TiO₂ (Anatase) Nanoparticles. *J. Phys. Chem. C* **2007**, *111*, 14925–14931.

(59) Lindström, H.; Södergren, S.; Solbrand, A.; Rensmo, H.; Hjelm, J.; Hagfeldt, A.; Lindquist, S. Li⁺ Ion Insertion in TiO₂ (Anatase). 2. Voltammetry on Nanoporous Films. *J. Phys. Chem. B* **1997**, *101*, 7717–7722.

(60) Conway, B.; Birss, V.; Wojtowicz, J. The role and utilization of pseudocapacitance for energy storage by supercapacitors. *J. Power Sources* **1997**, *66*, 1–14.